The Development of Global Probabilistic Propagation Look-Up Tables for Infrasound Celerity and Back-Azimuth Deviation

by Emily A. Morton and Stephen J. Arrowsmith

INTRODUCTION

Determining the source location, or associating detections of infrasound signals, is made complicated by the need for time-dependent information about the characteristics of the atmospheric medium through which the signal travels. The wind and temperature have a strong influence on the propagation of the wave, and these physical properties can vary significantly spatially and temporally (Garcés *et al.*, 1998; Drob *et al.*, 2003, 2010). Of particular importance for association and location is to have some constraints on the celerity (horizontal distance from source to receiver divided by travel time of sound wave) and the back-azimuth deviation (bias in the recorded back azimuth at an array due to wind). If one could model the celerity and back-azimuth deviation for a given observation, one could in principle determine the precise source location and origin time using the observed arrival time and celerity to obtain the range and the back-azimuth deviation to obtain the azimuth. A major challenge in infrasound monitoring is to model the celerity and back-azimuth deviation in such a way that the uncertainty in the atmospheric specification at any given instance in time is accounted for. This is particularly pertinent to detecting, associating, and locating global infrasound sources using the International Monitoring System (IMS) infrasound network; a global network including infrasound arrays for verification of the Comprehensive Nuclear-Test-Ban Treaty with 60 total (47 currently installed) infrasound stations (e.g., Christie and Campus, 2010; Nippress *et al.*, 2014). Having a set of prior information for a given area can aid in determining if one can expect detections at a certain azimuth and distance from a source and provide constraints on the characteristics of those detections. In addition, having information corresponding to previous atmospheric conditions can be used to improve source locations. For example, the use of physics-based modeled priors (Marcillo *et al.*, 2014) and data-based priors (Nippress *et al.*, 2014) to constrain celerity values at specific distances and azimuths from the source improved the location precision over use of a uniform prior distribution when implemented with a Bayesian location algorithm (Modrak *et al.*, 2010).

Because location precision, as well as detection and association of detections can benefit from parameter information based on previous atmospheric conditions, it would be preferable to always use such parameters. It would be tedious and time consuming, however, for the user to have to generate a set of prior parameter values for each new event analyzed. Here, we develop sets of priors for celerity and back-azimuth deviations (examples for back-azimuth deviations are not shown due to a lack of adequate ground-truth data for validation) at many node locations around the globe that can be used not just with the IMS network but any smaller scale networks located near the node locations as well. In addition, we develop a set of attenuation priors to be used specifically for work with the IMS network. For a specific user-specified research location, the celerity, back-azimuth deviation, and attenuation prior distributions can be used from the nearest global node.

DEVELOPMENT OF PHYSICS-BASED PRIORS USING PROPAGATION MODELING

To generate the prior celerity and back-azimuth deviation distributions, we use a 3D generalization of the geometric acoustics (GeoAc) approximation to model propagation developed by Blom and Waxler (2012) with calculations in Cartesian coordinates. We first compare the GeoAc propagation modeled celerity with that of the tau-p approximation for propagation (Garcés *et al.*, 1998; Drob *et al.*, 2010), used to generate the physics-based priors used by Marcillo *et al.* (2014). In addition, we compare these with observations that were used to generate data-based priors by Nippress *et al.* (2014) to ensure that the generated priors accurately represent the locations. The data used were rocket-motor detonation signals at the Utah test and training range (UTTR), a site of one of the main sources of infrasound signals in the western United States (Hedlin and Walker, 2013; Drob *et al.*, 2013; Nippress *et al.*, 2014).

Implementation

For both the GeoAc and tau-p propagation models, we use ground-to-space (G2S) profiles (Drob *et al.*, 2003, 2010) over the year 2010, a total of 2391 profiles each corresponding to a different time for the UTTR location. The G2S fields were computed for this time period based on the National Oceanic and Atmospheric Administration (NOAA) Global Forecast System (GFS) analysis fields below 35 km (Kalnay *et al.*, 1990), the National Aeronautics and Space Administration (NASA) MERRA analysis fields (Rienecker *et al.*, 2011) between 25 and 75 km, and the National Research Laboratory

doi: 10.1785/0220140124

mass spectrometer incoherent scatter/horizontal wind model (HWM07) empirical upper atmospheric model above that (e.g., Picone *et al.*, 2002; Drob *et al.*, 2008). The profiles range in altitude from 0 to 180 km, with increments of 200 m. For both models, we shoot rays at azimuths from 0° to 330° in increments of 30° and at inclination angles from 2° to 50° in increments of 2°, similar to the implementation by Marcillo *et al.* (2014). The simulations presented in this paper are range independent. Although range-dependent simulations would be preferable, the goal of this paper is primarily to develop the framework for the representation of the atmospheric state via a set of look-up tables. We recommend the development of range-dependent priors as a topic for future research but note that this requires massive computational resources for full range-dependent modeling over global scales using large ensembles of models. Once the model arrivals have been calculated, we limit the model results to 10 ray bounces and limit the turning elevation to ≤ 70 km to allow for only stratospheric returns and to better match restrictions of the observed data. In addition, we limit the date of analyzed G2S profiles to 15 May through 31 August, to correspond to the date range used for analysis with the recorded data (Nippress *et al.*, 2014). The recorded data analyzed in Nippress *et al.* (2014) used signals from UTTR on sensors from the IMS, additional four-element infrasound arrays, and seismic data from the USArray Transportable Array spanning 15 May through 31 August of 2004–2008. Arrival time picks were made on the largest peak-to-peak arrival of the signal. Although the data are from years 2004–2008, we chose the year 2010 for the G2S models to have the most recent year with consistent 6 h intervals to have the most concise data. Differences in year should not affect differences in model and data arrivals, as the changes tend to be seasonal. It has been shown in numerous studies that the G2S model contains more accurate specifications of the atmosphere for any given instance in time than climatological models such as HWM07 (e.g., Arrowsmith *et al.*, 2013). We use G2S under the assumption that the stochastic properties of the atmosphere are better represented using a more accurate set of profiles that contain more detailed specifications, particularly in the troposphere. The goal is to reduce the higher fidelity G2S model to a set of probability distributions that encapsulate this higher accuracy at any given snapshot in time through the development of stochastic models.

To compare the model results with the observed data, we analyzed celerity distributions as a function of range for azimuths in the western quadrant relative to the source (225°–315°, defined by Marcillo *et al.*, 2014 and Nippress *et al.*, 2014), in which the majority of the arrivals occur due to the stratospheric winds blowing east–to–west during summer months (e.g., Balachandran *et al.*, 1971; Whitaker and Mutschlecner, 2008; Hedlin and Walker, 2013; Nippress *et al.*, 2014). For both model and data distributions, we group celerity observations at the corresponding azimuths into range bins spanning 50 km and ranging from 0 to 1000 km from the source. Within each range bin, we then group the corresponding celerity values into 100 bins, the ranges and bin size varying slightly for each distribution (0.259–0.344 km/s with width 0.000859 km/s for the observed data; 0.283–0.356 km/s with width 0.000732 km/s for GeoAc; 0.283–0.339 km/s with width 0.000562 km/s for tau-p), and fit each with a Gaussian mixture model (GMM). These GMM parameters are projected to celerities from 0.26 to 0.36 km/s with bin width 0.0001 km/s for each distribution to ensure comparison on the same scale.

GMM Method

Because the calculated priors will potentially be used to aid location and association analysis, it would be easier and computationally less expensive to store a few parameters to be used in some function that would describe the data, rather than storing the entire distribution of ray arrival frequency at each celerity value. Calculating the GMM of the distribution allows us to store a few parameters that describe the GMM rather than the distribution itself.

Once the observations and model results have been grouped by azimuth and range, we find the best-fitting celerity Gaussian distribution or GMM using maximum-likelihood estimation. We define the prior distribution in a given range bin f_{x_i} for a set of possible celerities $\mathbf{x}$ as the sum of Gaussian probability density functions (PDFs):

$$f_{x_i}(\mathbf{x}) = \pi_1 \times f_1(\mathbf{x};\mu_1,\sigma_1) + \pi_2 \times f_2(\mathbf{x};\mu_2,\sigma_2) + \pi_3 \times f_3(\mathbf{x};\mu_3,\sigma_3), \quad (1)$$

in which π_n is a weight such that $\pi_1 + \pi_2 + \pi_3 = 1$, and f_1, f_2, and f_3 are Gaussian PDFs with corresponding means and standard deviations μ_n and σ_n, respectively. If only one Gaussian PDF is needed to describe the prior distribution, $\pi_1 = 1$ and the terms $\pi_2 \times f_2(\mathbf{x};\mu_2,\sigma_2)$ and $\pi_3 \times f_3(\mathbf{x};\mu_3,\sigma_3)$ are both zero.

We implement this by fitting the celerity distributions in each range bin with at least three ray arrivals with models for one Gaussian distribution ($\pi_1 = 1$, the other terms are zero), a combination of two weighted Gaussian distributions ($\pi_1 + \pi_2 = 1$, the third term is zero), and a combination of three weighted Gaussian distributions ($\pi_1 + \pi_2 + \pi_3 = 1$) indicating a minimum for the diagonal of the covariance matrix as 1×10^{-6}. We then find each fit type's Akaike information criterion (AIC) and store the mean(s) and standard deviation(s), whether for one, two, or three distributions and associated weights, corresponding to the lowest AIC value (Figs. 1 and 2). Figures 1 and 2 show the GMMs adequately fit the model and data distributions and can be used in place of the full distribution, which greatly decreases the storage needed.

COMPARISON OF REGIONAL PHYSICS-BASED MODEL AND DATA PRIORS

For a signal recorded at some distance from an explosion source, the recorded time series can be constructed, in the high-frequency limit, as the superposition of rays from different paths (multipathing). By measuring the time of peak amplitude on the waveform, one can conceptualize this as corresponding to the time of highest ray density (neglecting variations in absorption

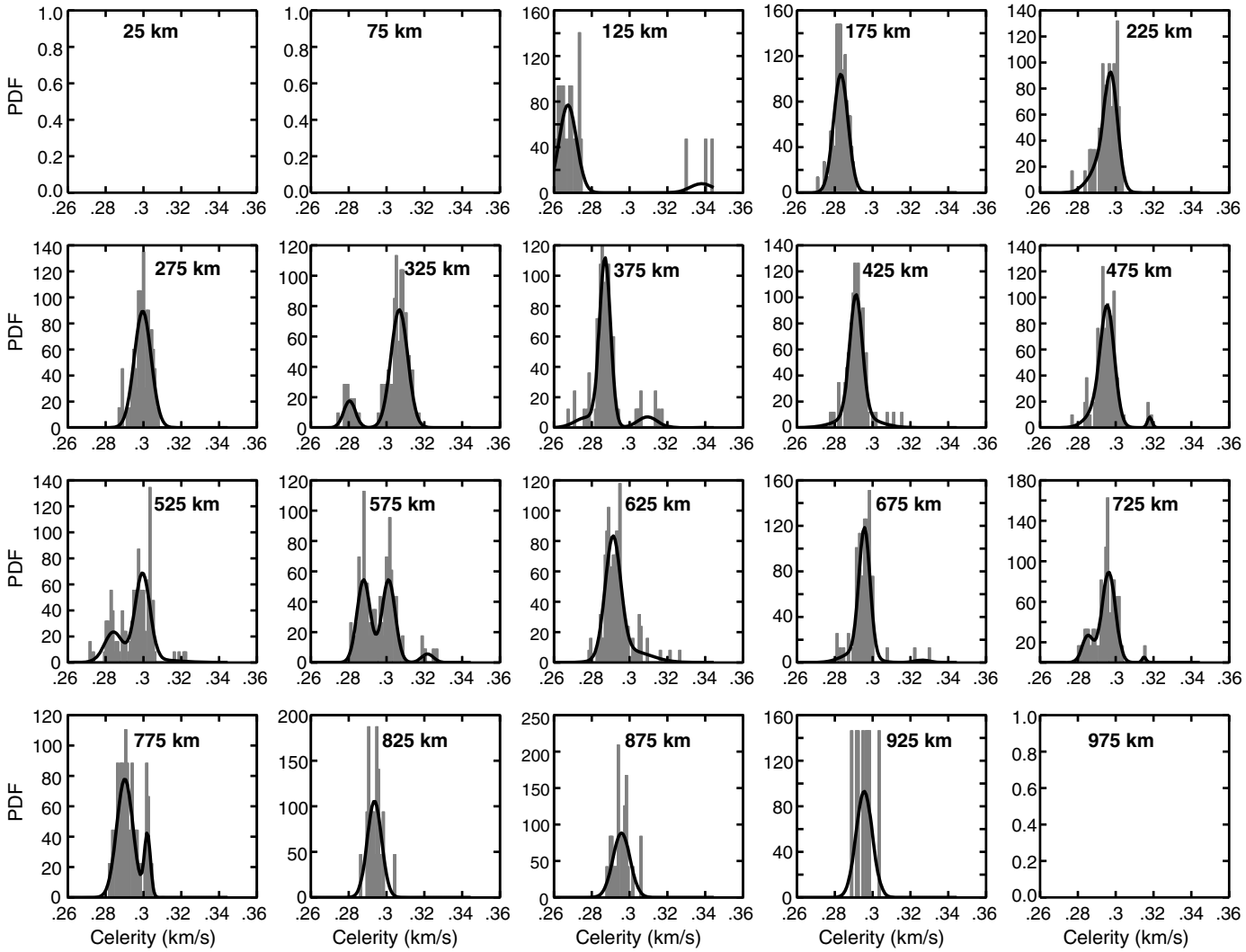

▲ **Figure 1.** Celerity probability density function (PDF) histograms of observed data from Utah test and training range from Nippress *et al.* (2014) with best-fitting Gaussian PDF distribution(s) model (black lines). Arrival times were picked at the largest peak-to-peak arrival and are dominantly stratospheric. Each subplot represents a different 50 km range bin with the title indicating the bin center.

along different ray paths) for a given source–receiver path. In this section, we compare GMMs extracted from histograms of measurements of the celerity at peak amplitude with GMMs extracted from histograms of predicted celerities based on ray theory. The atmospheric models used in generating the ray-based celerity histograms are chosen to represent the time periods corresponding to the observations.

Comparing the GMMs of the model results and data (Fig. 3) shows that the tau-p and GeoAc models are in very good agreement with each other in the majority of range bins and only exhibit significant differences at short ranges (e.g., 175 km, there are no tau-p predictions at closer ranges). This difference is due to the numerical implementation of the tau-p method whereby very-low-altitude ducts are not accurately predicted using the vertical parameterization we chose (125 m), whereas GeoAc is formulated in ray coordinates and is therefore better resolved for low-altitude refractions. Finer resolutions would better capture these very-low-level ducts but increase the computation time significantly. The two models agree well with the observed data in some of the range bins, such as 225, 275, and 475 km. In most range bins, however, the Gaussian components of the models only partly match those of the observed data. For example, in the 325 km range bin the models match the larger peak of the observed data, but the observed data also has a smaller weighted secondary peak at slower celerities. At 375 km, this slower peak becomes more enhanced, that is, has a larger weighting, whereas the models are still showing a dominant Gaussian component at faster celerities. At 425 km, the models now show slower celerities that match those of the data. This suggests that the distances at which the dominant stratospheric return switches from uS_i to uS_{i+1} (following the nomenclature of Hedlin *et al.*, 2010) is poorly resolved. Similar discrepancies are seen at 525–675 km and 775–925 km as well. At 125 km, the GeoAc model is predicting faster, tropospheric arrivals, whereas the observed data is showing dominantly stratospheric arrivals. This is noted

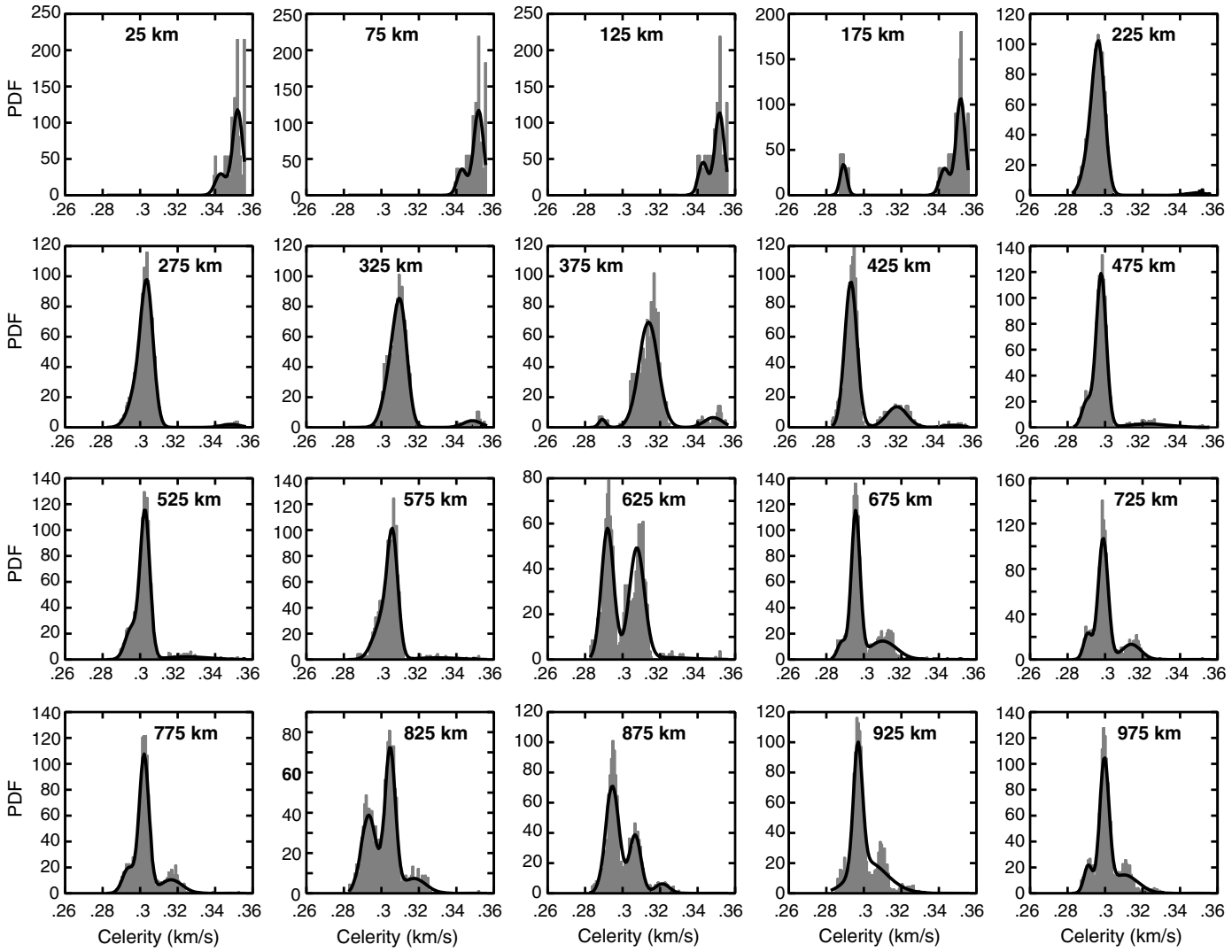

▲ **Figure 2.** Celerity PDF histograms of geometric acoustics (GeoAc) simulated data with best-fitting Gaussian PDF distribution(s) model (black lines). Each subplot represents a different 50 km range bin with the title indicating the bin center.

again at 175 km, although the GeoAc model also predicts smaller weighted stratospheric arrivals here and the tau-p model only shows the slower stratospheric arrivals. This is likely a reflection of the largest peak-to-peak picks from the observed data being stratospheric, and although tropospheric arrivals exist they are very small or not recorded. At the 25 km and 50 km range bins, the GeoAc model predicts tropospheric arrivals, but there were not enough stations at these ranges to provide observed data arrivals.

The faster model arrivals at certain range bins we see in Figure 3 may indicate that ray tracing through smooth G2S profiles does not correctly resolve the switch in stratospheric phase. Hedlin and Walker (2013), Drob *et al.* (2013), and Hedlin and Drob (2014) demonstrated that ray tracing through smooth G2S profiles successfully predicted the onset of arrivals, but not later arrivals or the duration of the signal, which may be the case here as well. They showed that by adding small-scale gravity wave perturbations to the G2S profiles, the newly predicted arrivals were more delayed and spread out in time, matching the complete duration of the signal, and also occurred at more extended ranges into areas that were previously predicted as shadow zones, but that contained observed arrivals (Hedlin and Walker, 2013; Drob *et al.*, 2013; Hedlin and Drob, 2014). Chunchuzov *et al.* (2014) was also able to predict arrivals that penetrate the shadow zone and other ranges that contain multiple stratospheric branches not predicted by smooth G2S profiles, as well as increased durations, by implementing range-dependent fluctuations in a single G2S profile with a pseudodifferential parabolic equation method. Finally, we note that the observed data was analyzed by picking the largest peak in the signal, which was not necessarily the first or only acoustic phase arrival of the signal. Therefore, it is possible that the models are predicting different phase arrivals than were picked or all phase arrivals.

We test the latter of the possible discrepancy explanations by choosing one of the shots observed at UTTR and repicking the waveforms to reflect all phase arrival peak times rather than

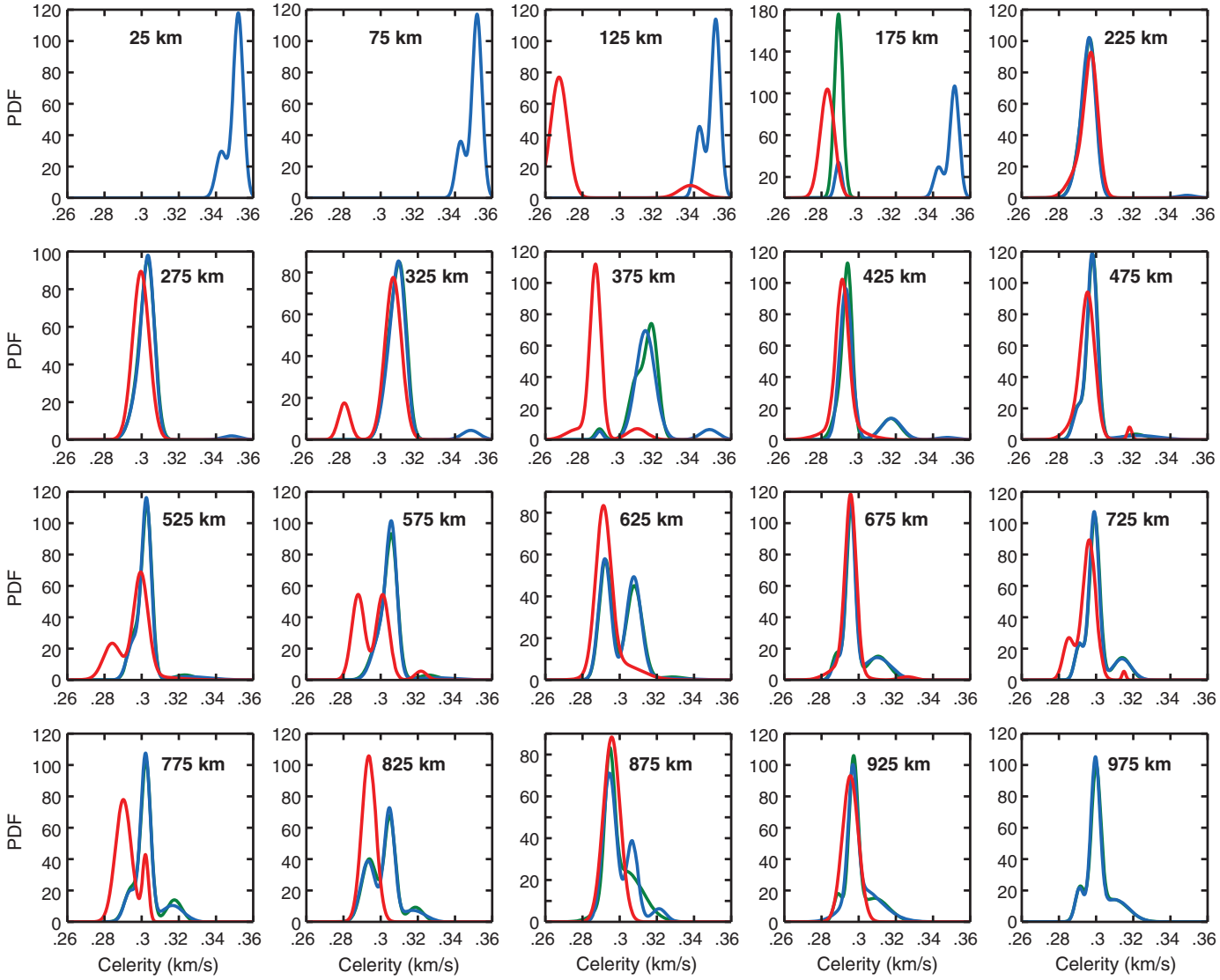

▲ **Figure 3.** Gaussian PDF distribution models describing observed data (red line) and simulated data (tau-p: green line, GeoAc: blue line). The two simulated data models are in good agreement with each other and in partial agreement with the observed data model.

the time of the overall maximum peak. We chose a shot on 1 August 2007 as it had the most stations picked of all the shots. Using the same seismic stations that were initially used to pick the shot arrival times, we picked the peak of all visible arrivals at each station (Fig. 4). These new picks were compared with the original picks from the selected shot and the GeoAc simulation for 1 August 2007 (Fig. 4). Four G2S profiles were used to generate the GeoAc model, distributed in 6 h intervals, and rays were shot at the previously defined azimuths. The inclination angle interval was decreased from 2° to 0.2° to generate a sufficient amount of arrivals, now that only one day is being used. We focused on ranges of 200 km and greater, as closer ranges had little to no arrivals for adequate analysis.

The new picks, which reflect picking the arrival time of the peak of all possible phase arrivals, tend to match all original picks and model components and in some cases create extra, unmatched components. In one of the previous problem ranges, 775 km, the all-phase picks show arrivals over the range of slower original picks and faster model predictions. Continuing into 825 km, the all-phase picks again show arrivals at both the slower celerities picked originally and faster celerities predicted by the model. In another previous problem range, 375 km, although there is no model for this smaller time range, the all-phase picks agree with the two groups of celerities indicated by the original picks.

The above results suggest that the GeoAc model can be used to represent a given location and generate prior values in most range bins. In the problem range bins, the models are only predicting the earlier, or faster, phase arrivals, rather than the highest ray density or all-phase arrivals. This agrees with the conclusion from the analysis of Hedlin and Walker (2013), Drob *et al.* (2013), and Hedlin and Drob (2014) that smooth G2S profiles match the onsets of signals. It is more likely, however, that the arrival-time picks made and used for infrasonic

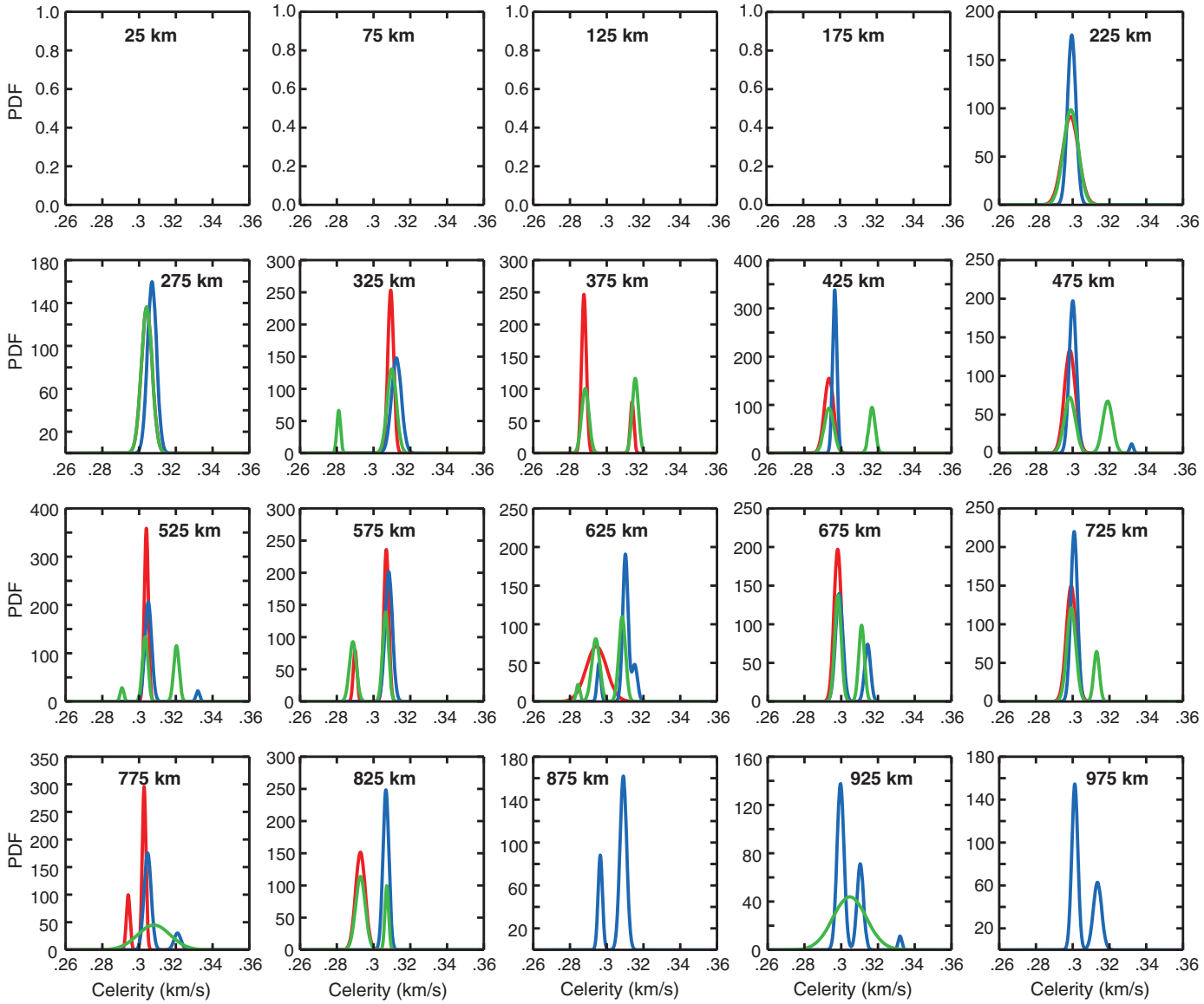

▲ **Figure 4.** Gaussian PDF distribution models describing original picks (red line), new peak time picks for all arrivals (green line), and GeoAc model (blue line) for 1 August 2007. At most ranges, using all arrivals adds extra celerity peaks that are not predicted by the model, and the model tends to predict the faster arrivals and miss a switch to a slower stratospheric arrival. At 675 km, however, the all arrival picks are in better agreement with the model.

location estimation will be peak times, as the onset is not always easily determined. Therefore, although the model matches well in most range bins and is acceptable for use now, it would be better to implement small-scale structures into the G2S profiles in the future to acquire more accurate model fits, as was demonstrated in other studies (e.g., Hedlin and Walker, 2013; Drob *et al.*, 2013; Chunchuzov *et al.*, 2014). It is worth noting that the GeoAc simulations for 1 August 2007 and 1 August 2010 with the same ray-shooting parameters (azimuth and inclination angle) are in very good agreement, and so the model is translatable over different years during the same month/daytime period. In other words, the statistical properties of the simulated data does not have to be generated on the exact date of the shot to match the statistical properties of the observed data but can be generated using G2S models from previous or later years.

For simplicity, the comparisons between measured and predicted celerity models in this paper have been qualitative. Such a qualitative approach is adequate when the goal is simply to identify where research and development is needed for improvements in modeling. The utilization of more rigorous quantitative measures, such as the Kullback–Leibler distance, for validation of the GMMs is left for future research. However, one advantage of using GMMs, as we have done in this paper, is that there is a range of existing statistical measures that can be leveraged for this purpose.

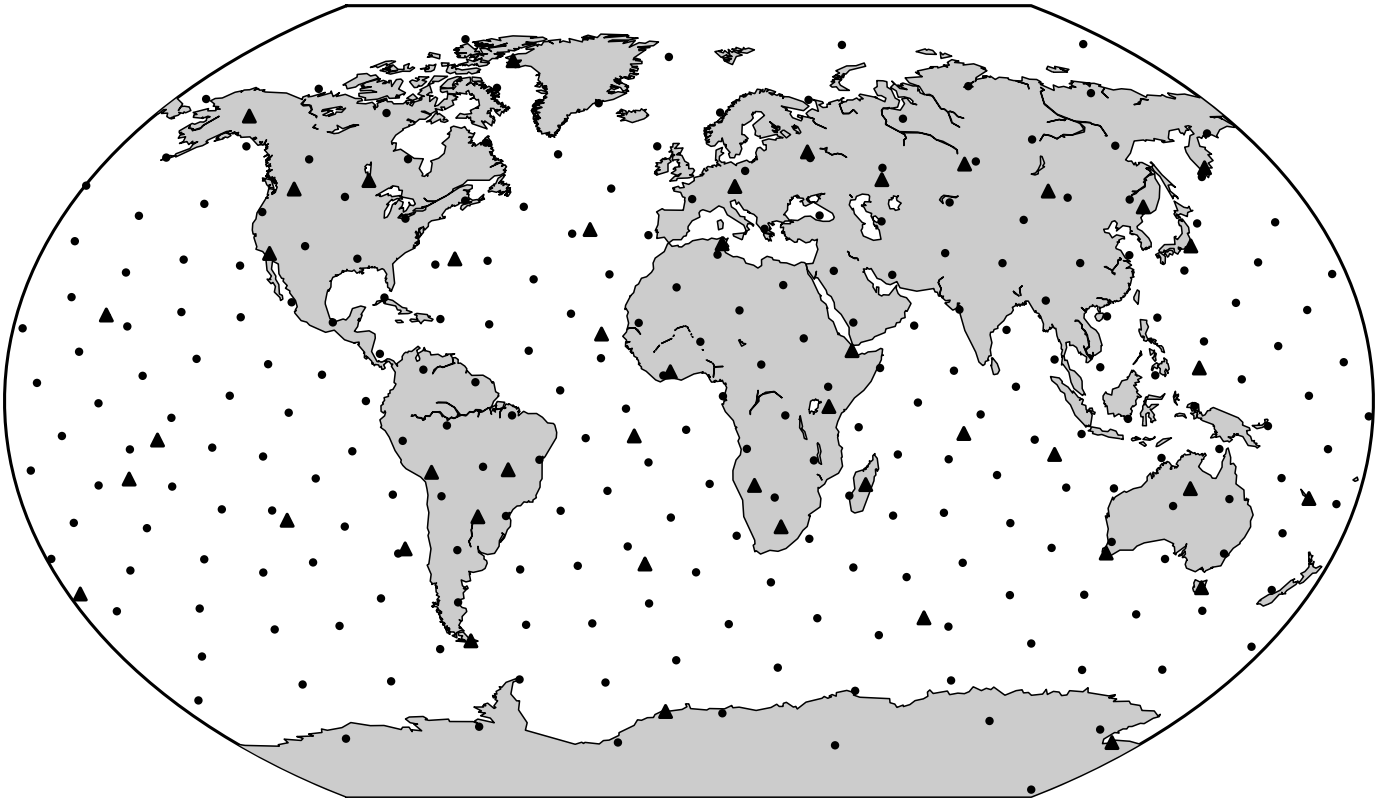

▲ **Figure 5.** Locations of 250 nodes used to generate prior distributions (dark gray dots) and 45 International Monitoring System (IMS) stations used (47 stations are installed, but only 45 were available to us) for calculating attenuation (black triangles). Nodes are equally spaced at approximately 1459.58 km. Prior distributions can be used by choosing the nearest node to a given even location or interpolating between nodes.

SUMMARY OF GLOBAL PRIORS

We establish 250 nodes approximately equally spaced at ~1459.6 km for locations around the globe for which to generate a set of priors (Fig. 5). For this portion of the project, we use only profiles that are evenly distributed at 6 h intervals to ensure equal weighting, from November 2009 through October 2010; a total of 1439 times. November and December 2010 had time gaps that were too large between profiles and were replaced by the same months in 2009. In this portion, we only used the GeoAc model but again shoot rays at azimuths from 0° to 330° in increments of 30° and at launch angles from 2° to 50° in increments of 2°.

To generate the GMM fits for the global priors, we separate the ray arrivals by month, azimuth, and 50 km range bins at each node location (Fig. 5). Unlike the UTTR simulations, we do not limit the arrivals by turning elevation ≤70 km, as we do not need to compare the arrivals with limited data. Rather, we limit tropospheric arrivals (turning elevation <30 km) to 10 ray bounces, stratospheric arrivals (turning elevation z, 30 km ≤ z < 60 km) to within 10,000 km from the source, and thermospheric arrivals (turning elevation z, 60 km ≤ z < 120 km) to 1 ray bounce. This adjustment reflects our expectation of observing few tropospheric arrivals at the closest ranges, mostly stratospheric arrivals over the observed ranges, and no thermospheric returns at long ranges due to high absorption in the thermosphere (e.g. Sutherland and Bass, 2004). For each location–month–azimuth–range bin, we find the best-fitting GMM for the celerity distribution as we did for UTTR, allowing for one, two, or three components, and stored the model parameters corresponding to the lowest AIC for bins with at least three ray arrivals. In addition, we calculate a back-azimuth deviation for each ray based on the original shooting azimuth and the resulting ray azimuth and similarly fit a GMM for the back-azimuth deviation distribution in each location–month–azimuth–range bin. From this, we acquire a set of celerity and back-azimuth deviation prior distributions for each location–azimuth–month–range bin combination.

For any given node–azimuth–month–range combination, there tends to be less than 500 ray bounce points predicted, but in some cases the number of bounce points can be as high as 7993. We examine an example of celerity priors by choosing a location, month, and azimuth and varying one of these parameters whereas keeping the rest constant for ray bounce points within 550–600 km of the source (Fig. 6). To vary the location, we chose every node within a longitude band between 110° W and 100° W and examined the GMM prior distributions for January and due east (90°) from the source. Figure 6a shows the prior PDFs added to their corresponding latitude (so

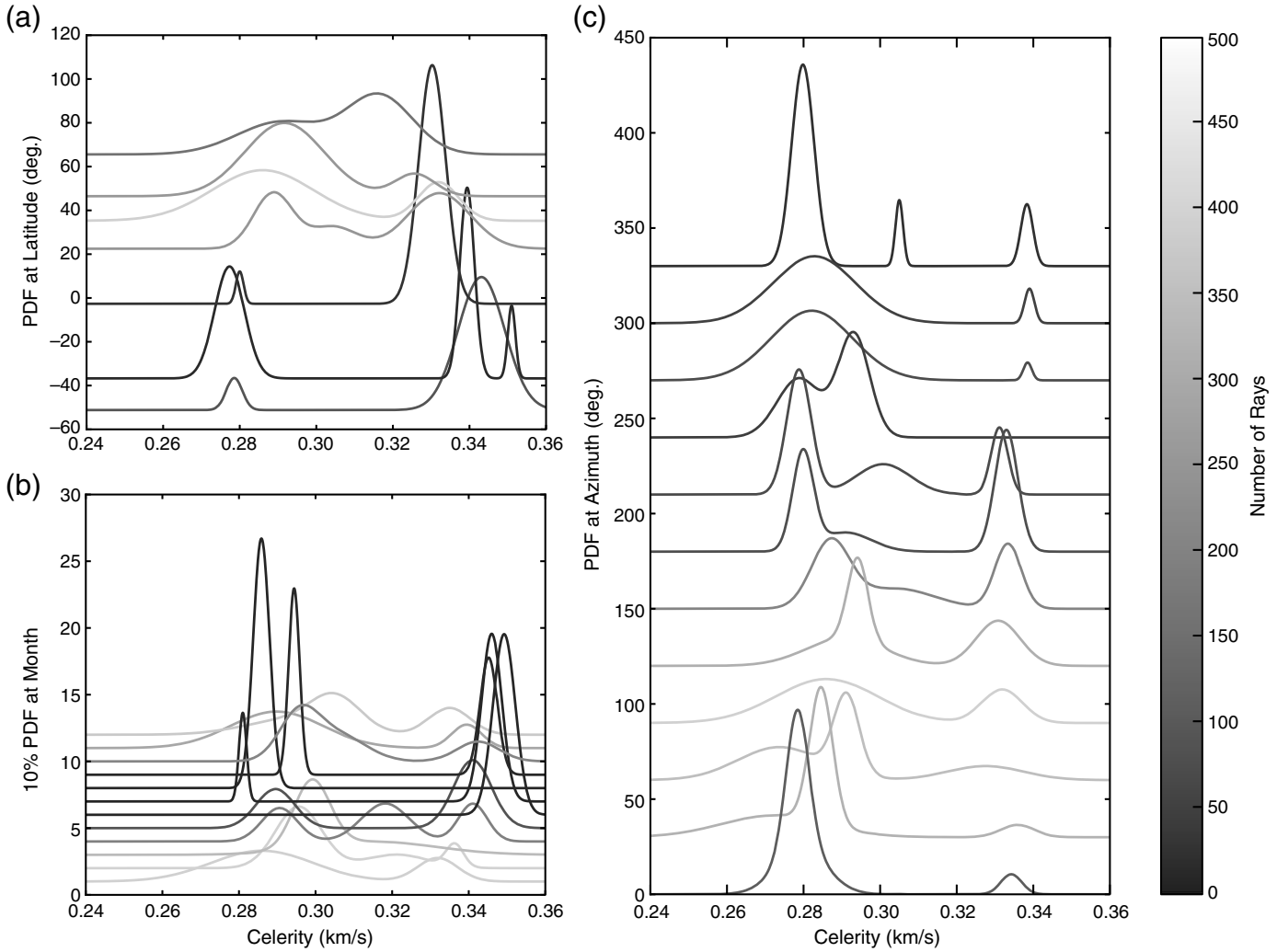

▲ **Figure 6.** Celerity prior Gaussian mixture model distributions varying with location, time, and azimuth with colors relating to the number of ray arrivals in the corresponding location–month–azimuth–range bin. All plots correspond to arrivals within 550–600 km from the source. (a) The prior PDFs are added to their latitude value for all node locations between longitudes of 110° W and 100° W for the month of January and at an azimuth 90° from the node. (b) Prior PDFs from the location in New Mexico from Figure 5 (node 28) and keeping the azimuth at 90° varies the month analyzed. PDFs in the plot are scaled by 10% for better visibility and added to the number of the corresponding month (e.g., a PDF value of 0 in January would be at 1). (c) We again use the New Mexico location and January and vary the azimuths from the source.

that a value of zero in the PDF is at the location's latitude). In the northern hemisphere, for January and the longitude band centered on −105° W, the different GMM components are wide and merge together to cover a large region of celerities from ∼0.27 to ∼0.35 km/s, whereas in the southern hemisphere the components are more condensed to particular celerity values and separate. Additionally, we see that there are far more ray arrivals in the northern hemisphere (to be expected for propagation at 90°: stratospheric winds blow toward the east in the winter in the northern hemisphere). Similarly in Figure 6b, we chose a node located northwest of Albuquerque, New Mexico, and vary the month of prior distributions with azimuths to the east. The PDF is scaled to 10% and added to the respective month. Here, we see that the months during which the winds are blowing toward the east (winter months) have more ray arrivals and have a broader range of celerities with wider GMM components. The summer months have fewer arrivals and more concentrated celerity values. This seasonal difference in distributions results from the fact the summer stratospheric wind jet peak is weaker and occurs at higher altitude (∼70 km) than the wintertime wind jet, which is lower (55 km), stronger, and certainly more variable. In Figure 6c, we use the same New Mexico location and the month of January and add the PDFs to the azimuth at which the rays were shot. As expected, more ray arrivals are observed to the east (30°–150°). GMM components broadly cover celerities for 60°–210° and are more concentrated for 270°–30°. Very generally from this example, we can say that at the time and in the

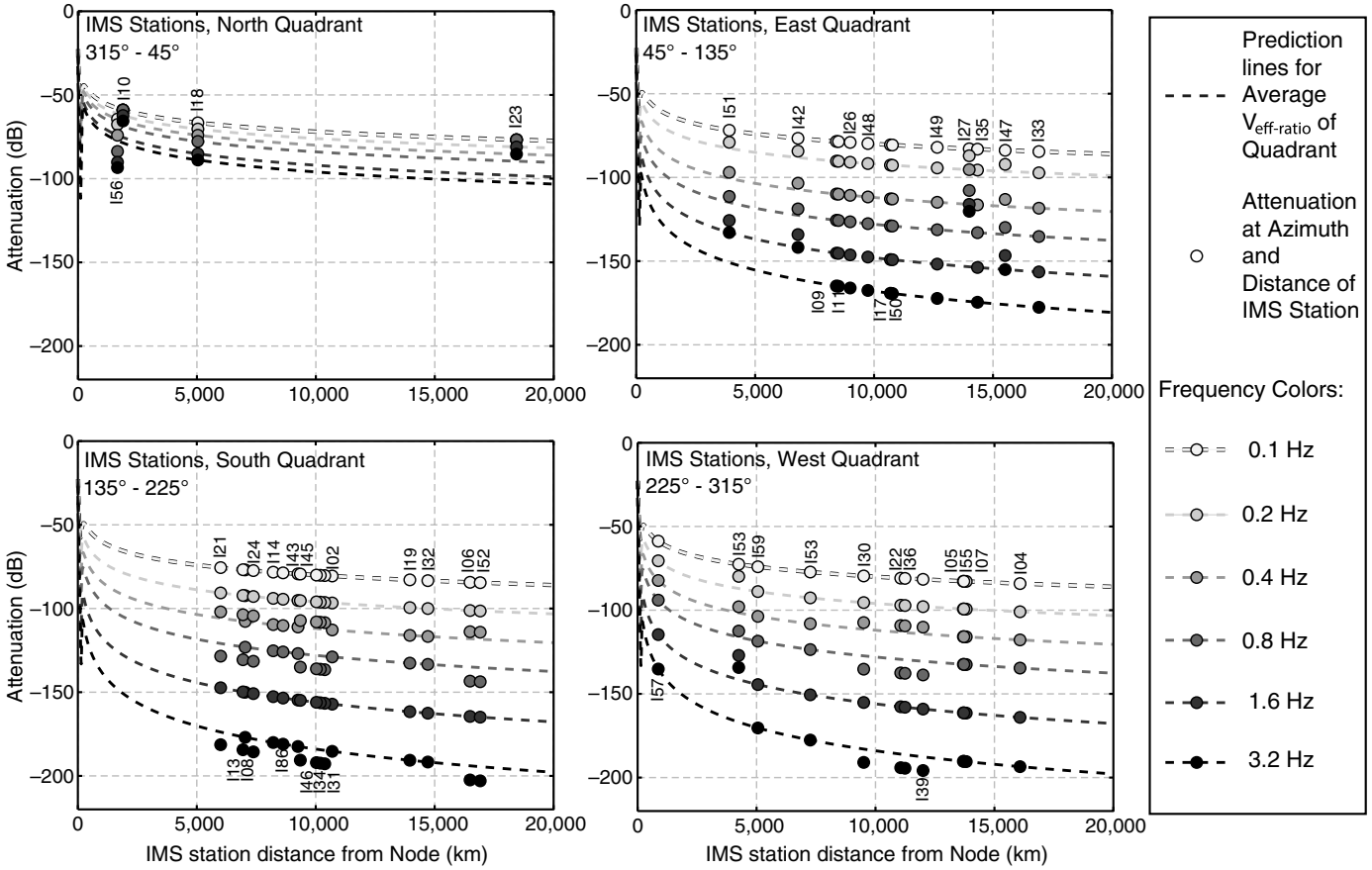

▲ **Figure 7.** Attenuation from node 28 (New Mexico) to IMS stations (dots) separated by directional quadrants with curves based on average $V_{\text{eff-ratio}}$ in each quadrant (dotted lines) for January. Attenuation prediction lines and values at each station are colored by frequency. The average $V_{\text{eff-ratio}}$ values are <1 for east, west, and south, and ~1 for north.

direction the winds are blowing, we see more rays and they cover a broader range of celerities.

Another parameter that will help in evaluation of detections and association is how the signal is attenuated from each node to 45 of the 47 IMS network stations that will be used for detection and signal location (Fig. 5; Only 45 locations available at the time of this paper). Instead of using geometric ray theory, as for the celerity and back-azimuth deviation prior distributions, we use equation (2) of Le Pichon *et al.* (2012) to calculate the attenuation from each node to each IMS site, which is based on numerical simulations and incorporate small-scale fluctuations in horizontal wind velocity. We note that, although this equation makes a number of assumptions, and is limited to stratospheric arrivals, it is currently the best available analytical equation for transmission loss as a function of frequency and range. We use the same frequencies (0.1, 0.2, 0.4, 0.8, 1.6, and 3.2 Hz) and corresponding values for parameters α, β, δ, and σ with the node–IMS site distances and $V_{\text{eff-ratio}}$ values pertaining to the direction from the node to the site calculated from the G2S models. We calculate an attenuation value for each node–month–frequency–IMS site combination. In Figure 7, we show the resulting attenuation for each IMS site relative to the New Mexico node and separated by directional quadrant (defined in Marcillo *et al.*, 2014 and Nippress *et al.*, 2014) for January, with dashed curves that correspond to the average $V_{\text{eff-ratio}}$ calculated from the specific azimuths of the IMS stations within each quadrant. The east, west, and south quadrants all have average $V_{\text{eff-ratio}}$ values < 1, indicating rays will be refracted upward. As was noted by Le Pichon *et al.* (2012), when $V_{\text{eff-ratio}} < 1$, the attenuation strongly increases with frequency. This is shown in the east, west, and south quadrants, as opposed to the north quadrant, where the average $V_{\text{eff-ratio}}$ is ~1 and the attenuation curves for all frequencies are more tightly distributed. In addition, whereas the curves are equivalent at 0.1 Hz, at higher frequencies the attenuation is greater to the west and south than to the east (a difference between directions on the order of ~6–8 dB at 1.6 Hz and ~12–17 dB at 3.2 Hz). The increase in attenuation from the east to the south and west also increases more so with distance; at 0.2 Hz the difference between the east and south/west curves increases from 3 dB at 1000 km to 4.3 dB at 20,000 km, and at 3.2 Hz the difference between the east and south/west curves increases from 12 dB at 1000 km to 17.2 dB at 20,000 km. The larger attenuations to the south and west relative to the east may reflect the eastward wind direction in January, however, the curves at 0.1, 0.4, and 0.8 Hz are

equivalent for all three directions. Using these attenuation parameters for all the nodes and at every month, one can estimate if the amplitude of a signal is detectable on a particular IMS station if coming from a particular source during a certain month and source frequency.

CONCLUSIONS

In this study, we used ray tracing through G2S profiles in an attempt to develop a set of prior celerity and back-azimuth deviation distributions (examples of celerity are shown, but examples of back-azimuth deviation are not) and calculate attenuation tables that adequately describe a given location to be used to aid detection and association of detections between stations, as well as improve source locations.

We first tested the model ray tracing at the UTTR site and compared the predicted celerities with observed UTTR data (Nippress *et al.*, 2014). In this example, we found the model results can be described by a Gaussian or a weighted combination of two or three Gaussians, and the GeoAc and tau-p results are in very good agreement with each other. This ensures that we can use the GeoAc method for generating prior distributions in place of the previously used tau-p method (Marcillo *et al.*, 2014) and also ensures that we can store a few parameters pertaining to the Gaussian distributions for each prior distribution, rather than storing an extensive set of ray arrival frequencies for each possible parameter value at each location, range, azimuth, and time. In comparison to the observed data at UTTR, we find that for a few ranges the models predict faster arrivals than were picked, but most range bins agree well with the data. At the moment these comparisons are qualitative, and we leave more rigorous quantitative comparisons for future work. Therefore, the GeoAc ray-tracing method generates predicted arrivals that adequately represent the location, but future implementations would benefit from incorporating small-scale structure into the G2S profiles and performing range-dependent propagation simulations. It is important to note that a limitation with constructing probabilistic propagation models on the basis of previous atmospheric specifications is for unusual atmospheric conditions that are not captured in the priors. For such unusual atmospheric scenarios, such as sudden stratospheric warming events (e.g., Assink *et al.*, 2014), the use of additional constraints on unusual atmospheric conditions may be necessary to avoid the use of inappropriate priors. The use of range dependence is particularly important for paths out to 1000 km in which the propagation paths may span different environments such as desert, mountain, or oceans. Future research is needed to develop and validate range-dependent priors that properly account for these effects.

We apply the ray-tracing and attenuation calculations for each node-to-IMS station for 250 equally spaced locations around the globe. Examining one example node in New Mexico, we can confirm that we see more ray arrivals to the east during the winter months, as to be expected. In addition, there is slightly more attenuation at higher frequencies to the west and south of the node and more spread in attenuation with increasing frequency to the east, west, and south of the node. These look-up tables for 250 locations can be used to determine if a signal should be detectable or if the observed celerity is expected from a particular source region and to aid in detection association between stations, as well as improve source locations around the globe.

ACKNOWLEDGMENTS

We are grateful for reviews from David Fee and an anonymous reviewer, which helped us to clarify and strengthen this work. We thank Philip Blom for use of his geometric acoustics ray propagation code and input on the project, as well as David Green, Dale Anderson, Rod Whitaker, and Omar Marcillo for helpful feedback. We also thank Alexandra Nippress for providing Utah test and training range event picks and information used in Nippress *et al.* (2014) for comparisons. Data from the Transportable Array network were made freely available as part of the EarthScope USArray facility, operated by Incorporated Research Institutions for Seismology and supported by the National Science Foundation, under Cooperative Agreements EAR-0323309, EAR-0323311, and EAR-0733069. The GEOS-5 data utilized in conjunction with other data sources in the National Research Laboratory ground-to-space (G2S) atmospheric specification used in modeling was provided by the Global Modeling and Assimilation Office at National Aeronautics and Space Administration (NASA) Goddard Space Flight Center through the online data portal in the NASA Center for Climate Simulation. The National Oceanic and Atmospheric Administration (NOAA) Global Forecast System (GFS), also utilized in the G2S specifications, was obtained from NOAA's National Operational Model Archive and Distribution System, which is maintained at NOAA's National Climatic Data Center. This document is Los Alamos National Laboratory Publication Number LA-UR-14-24264.

REFERENCES

Arrowsmith, S. J., O. Marcillo, and D. P. Drob (2013). A framework for estimating stratospheric wind speeds from unknown sources and application to the 2010 December 25 bolide, *Geophys. J. Int.* **195,** 495–503, doi: 10.1093/gji/ggt228.

Assink, J. D., R. Waxler, P. Smets, and L. G. Evers (2014). Bidirectional infrasonic ducts associated with sudden stratospheric warming events, 119, 1140–1153, *J. Geophys. Res.* doi: 10.1002/2013JD021062.

Balachandran, N. K., W. L. Donn, and G. Kashack (1971). On the propagation of infrasound from rockets, *J. Acoust. Soc. Am.* **50,** no. 2, 397–404.

Blom, P., and R. Waxler (2012). Impulse propagation in the nocturnal boundary layer: Analysis of the geometric component, *J. Acoust. Soc. Am.* **131,** no. 5, 3680–3690.

Christie, D. R., and P. Campus (2010). The IMS infrasound network: Design and establishment of infrasound stations, in *Infrasound Monitoring for Atmospheric Studies*, Alexis Le Pichon, Elisabeth Blanc, and Alain Hauchecorne (Editors), Springer, Dordrecht, Netherlands, 29–76.

Chunchuzov, I., S. Kulichkov, O. Popov, and M. Hedlin (2014). Modeling propagation of infrasound signals observed by a dense seismic network, *J. Acoust. Soc. Am.* **135,** no. 1, 38–48.

Drob, D. P., D. Broutman, M. A. Hedlin, N. W. Winslow, and R. G. Gibson (2013). A method for specifying atmospheric gravity wavefields for long-range infrasound propagation calculations, *J. Geophys. Res.* **118,** 3933–3943, doi: 10.1029/2012JD018077.

Drob, D. P., J. T. Emmert, G. Crowley, J. M. Picone, G. G. Shepard, W. Skinner, P. Hays, R. J. Niciejewski, M. Larsen, C. Y. She, J. W. Meriwether, G. Hernandez, M. J. Jarvis, D. P. Sipler, C. A. Tepley, M. S. O'Brien, J. R. Bowman, Q. Wu, Y. Murayama, S. Kawamura, I. M. Reid, and R. A. Vincent (2008). An empirical model of the Earth's horizontal wind fields: HWM07, *J. Geophys. Res.* **113,** A12304, doi: 10.1029/2008JA013668.

Drob, D. P., M. Garcés, M. Hedlin, and N. Brachet (2010). The temporal morphology of infrasound propagation, *Pure Appl. Geophys.* **167,** no. 4, 437–453, doi: 10.1007/s00024-010-0080-6.

Drob, D. P., J. M. Picone, and M. Garcés (2003). Global morphology of infrasound propagation, *J. Geophys. Res.* **108,** no. D21, 4680, doi: 10.1029/2002JD003307.

Garcés, M. A., R. A. Hansen, and K. G. Lindquist (1998). Traveltimes for infrasonic waves propagating in a stratified atmosphere, *Geophys. J. Int.* **135,** 255–263.

Hedlin, M. A., and K. T. Walker (2013). A study of infrasonic anisotropy and multipathing in the atmosphere using seismic networks, *Phil. Trans. Roy. Soc. Lond. A.* **371,** no. 1984.

Hedlin, M. A. H., and D. P. Drob (2014). Statistical characterization of atmospheric gravity waves by seismoacoustic observations, *J. Geophys. Res.* **119,** no. 9, 5345–5363, doi: 10.1002/2013JD021304.

Hedlin, M. A. H., D. Drob, K. Walker, and C. de Groot-Hedlin (2010). A study of acoustic propagation from a large bolide in the atmosphere with a dense seismic network, *J. Geophys. Res.* **115,** no. B11312, doi: 10.1029/2010JB007669.

Kalnay, E., M. Kanamitsu, and W. E. Baker (1990). Global numerical weather prediction at the National Meteorological Center, *Bull. Am. Meteorol. Soc.* **71,** no. 10, 1410–1428.

Le Pichon, A., L. Ceranna, and J. Vergoz (2012). Incorporating numerical modeling into estimates of the detection capability of the IMS infrasound network, *J. Geophys. Res.* **117,** D05121, doi: 10.1029/2011JD016670.

Marcillo, O., S. Arrowsmith, R. Whitaker, D. Anderson, A. Nippress, D. Green, and D. Drob (2014). Using physics-based priors in a Bayesian algorithm to enhance infrasound source location, *Geophys. J. Int.* **196,** no. 1, 375–385, doi: 10.1093/gji/ggt353.

Modrak, R. T., S. J. Arrowsmith, and D. N. Anderson (2010). A Bayesian framework for infrasound location, *Geophys. J. Int.* **181,** 399–405, doi: 10.1111/j.1365-246X.2010.04499.x.

Nippress, A., D. N. Green, O. E. Marcillo, and S. J. Arrowsmith (2014). Generating regional infrasound celerity-range models using ground-truth information and the implications for event location, *Geophys. J. Int.* **197,** no. 2, 1154–1165, doi: 10.1093/gji/ggu049.

Picone, J. M., A. E. Hedlin, D. P. Drob, and A. C. Aikin (2002). NRLMSISE-00 empirical model of the atmosphere: Statistical comparisons and scientific issues, *J. Geophys. Res.* **107,** no. A12, 1468.

Rienecker, M. M., M. J. Suarez, R. Gelaro, R. Todling, J. Bacmeister, E. Liu, M. G. Bosilovich, S. D. Schubert, L. Takacs, and G.-K. Kim et al. (2011). MERRA: NASA's modern-era retrospective analysis for research and applications, *J. Clim.* **24,** 3624–3648.

Sutherland, L. C., and H. E. Bass (2004). Atmospheric absorption in the atmosphere up to 160 km, *J. Acoust. Soc. Am.* **115,** no. 3, 1012–1032.

Whitaker, R. W., and J. P. Mutschlecner (2008). A comparison of infrasound signals refracted from stratospheric and thermospheric altitudes, *J. Geophys. Res.* **113,** D08117, doi: 10.1029/2007JD008852.

Emily A. Morton
Stephen J. Arrowsmith
Los Alamos National Laboratory
EES-17 Geophysics Group
P.O. Box 1663
Mail Stop F665
Los Alamos, New Mexico 87545 U.S.A.
emorton@lanl.gov

Published Online 1 October 2014